Effects of local fiber orientation state on thermal-mechanical behaviors of composite parts made by large area polymer deposition additive manufacturing

Zhaogui Wang[1], Zhenyu Fang[1], Douglas E. Smith[2]

[1]Department of Mechanical Engineering, Dalian Maritime University, Dalian, China, 116000
[2]Department of Mechanical Engineering, Baylor University, Waco, TX, USA, 76798

Abstract

Short carbon fiber enhances the dimensional stability and material strength of composite parts created via large area polymer deposition additive manufacturing, which has been used for rapid fabrications of large-dimension composite parts and tooling. Nevertheless, the flow-induced fiber orientation formed during the material extrusion and deposition leads the deposited composites exhibit non-homogeneous thermal-mechanical behaviors. This study evaluates the fiber orientation state of a 20 wt.% CF-PEI composite fabricated by polymer deposition using the fully coupled flow/orientation approach. The material properties are computed by considering the deposited bead as heterogeneous segments with different local fiber orientation states. The heterogeneous thermal conductivity and expansion coefficient exhibit maximum local differences of 29% and 21%, respectively. The orientation-homogenized material properties are implemented to the finite element simulation for a large area additive manufacturing process of a single bead and notable differences are seen between results computed by employing the homogenous and heterogeneous properties.

Introduction

Large Area polymer deposition Additive Manufacturing (LAAM) is seen rapid growth in the area of composite manufacturing due to the high efficiency enabled by the screw-extruder-based material feeding system [1]. Large-dimension composites parts and tooling including the full-size car, boat or wind turbine blade mold are 3D printed directly through the LAAM technology with less cost in time and materials as compared to conventional methods [2-5]. The carbon fiber filled composites provide superior stiffness and low thermal expansion that enhance the mechanical performance of fabricated structures. Specifically, the discontinuous fibers re-orient as the material flow being extruded and deposited onto the material substrate and the resulting fiber orientation in the beads can be quite different locally as seen in Figure 1. Nixon, et al. evaluated the internal geometric effects of the extrusion nozzle on the fiber orientation alignment using Moldflow software (Moldflow Corporation, Framingham, MA, USA), where a convergent nozzle geometry was found to yield higher fiber alignment than a divergent designed nozzle [6]. Heller, et al. employed an axisymmetric 2D flow model via COMSOL (COMSOL Inc., Burlington, MA, USA) simulating the nozzle flow with a short section of free extrudate included, and found that the die swell at nozzle exit reduced the principal fiber orientation by ~20% [7]. Extended works based on Heller's model explored the non-Newtonian fluid rheology effects [8] and the screw swirling motion [9] on the resulting fiber orientation of an extrudate composite. Above mentioned studies are done using a weakly coupled formulation between the flow kinematics and fiber orientation evolution, where the presence of fibers is ignored during the

computation of the flow kinematics. In contrast, Beversta, et al. employed smoothed particle hydrodynamics method simulating the transient flow development during the planar deposition process [10], where the flow kinematics and fiber orientation were solved in a mutually coupled formulation. Under the same fully coupled scheme, Wang and Smith, on the other hand, applied the finite element approach evaluating the flow and fiber orientation fields in a nozzle-extrudate flow [11] and planar deposition flow [12], where a quasi-steady state of fiber orientation in the extruded composites was obtained for further material properties estimations. Computed results from prior studies (e.g., [7,8,11,12]) indicated that the fiber orientation pattern within the deposited beads has a direct effect on the material properties of the printed parts.

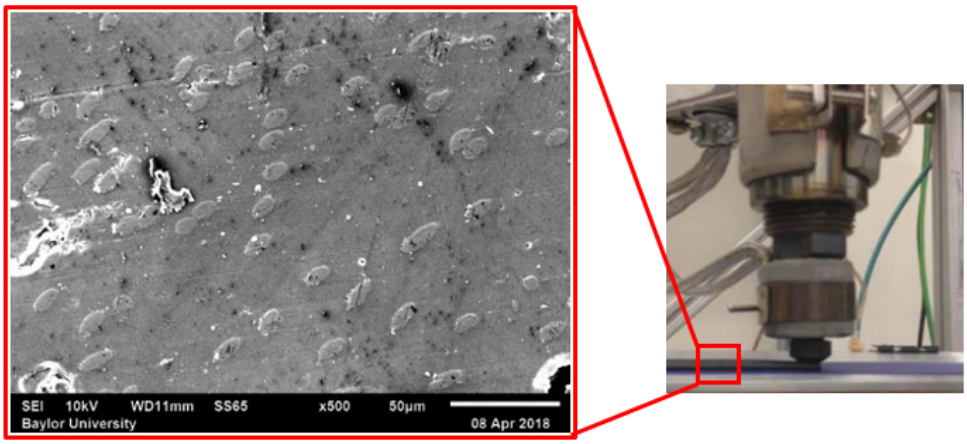

Figure 1. Complex local orientation across a composite bead extruded by LAAM.

Particularly, this study is interested in the effect of local fiber orientation within a bead on the material properties of the printed composites through LAAM systems. Firstly, the non-Newtonian flow kinematics and fiber orientation fields in a planar deposition flow domain are solved in a fully coupled formulation via the finite element method. The flow field is modeled using the power law model and the fiber orientation state is evaluated using the Advani-Tucker orientation tensor approach through the Folgar-Tucker fiber orientation evaluation equation with isotropic rotary diffusion and orthotropic fitted closure. Then, the material properties of a deposited bead are estimated through the orientation homogenization approach, including the elastic constants, coefficients of thermal expansion and thermal conductivity. The material properties estimation includes the effects of the locally different fiber orientation states. The transient thermal-mechanical history of the LAAM printing process of a single deposited strand is simulated via ABAQUS using the calculated properties.

Fully Coupled Flow/Orientation Analysis

Governing equations for modeling the fiber reinforced composite material flow for LAAM applications including the identifications of the flow fields of the molten material as well as the fiber orientation state within the flow suspension, which are introduced in this section.

Flow Kinematics Governing Equations

Properly identifying the flow fields of the composite melt flow ensures the evaluation of the flow-induced fiber orientation in the nozzle and free extrudates. Prior literature [6-9] addressed the nozzle flow characterization through a decoupled formulation, where the flow fields are solved as if no fibers present in the polymer melt. An isothermal, incompressible, and highly viscous creeping flow is elsewhere considered in prior related work [7], where the thermal gradients, inertia effect, and the time transient effect are neglected. Under these assumptions, the mass the momentum conservation equations of the flow field can be, respectively, written as [13]

$$\nabla \cdot \boldsymbol{v} = 0, \tag{1}$$

and,

$$\nabla \cdot \boldsymbol{\sigma} + \rho \boldsymbol{f} = 0, \tag{2}$$

where $\boldsymbol{v}$ is the velocity tensor, ρ refers to the density of the continuum, $\boldsymbol{f}$ refers to the body force tensor, and $\boldsymbol{\sigma}$ is the Cauchy stress tensor, which can be written as [13]

$$\boldsymbol{\sigma} = \boldsymbol{\tau} - \mathrm{P}\boldsymbol{I}, \tag{3}$$

where P is the pressure, $\boldsymbol{I}$ is the identity matrix, and $\boldsymbol{\tau}$ is the stress tensor associated shear deformation. The latter can be written with an anisotropic contribution from fiber orientation as [13]

$$\boldsymbol{\tau} = 2\eta \boldsymbol{D} + 2\eta N_p \mathbb{A} : \boldsymbol{D}, \tag{4}$$

where η is the viscosity of melt, and N_p is the particle number that characterizes the intrinsic anisotropic impacts of the fibers on the flow rheology. $\mathbb{A}$ is the fourth-order fiber orientation tensor which will be introduced in the following section. By employing the second part in Equation 4, the computations of flow and fiber orientation are coupled.

Fiber Orientation Governing Equations

Characterizing the fiber orientation kinetics for filled polymer systems in LAAM applications is of great importance as the final alignment of fibers in the deposited materials significantly determines the strength, stiffness and warpage of a printed part. Jeffery's Equation [14] first expressed the motion of a single rigid ellipsoidal particle. Folgar and Tucker [15] extended Jeffery's theory to analyze the interactions between fibers in a non-dilute fiber suspension. Further, Advani and Tucker [16] defined the fiber orientation tensor approach to quantify the fiber alignment state for concentrated suspension systems, which requires fewer independent variables than that of the Folgar-Tucker model[15]. The Advani-Tucker equation can be written as[16]

$$\frac{D\boldsymbol{A}}{Dt} = (\boldsymbol{W} \cdot \boldsymbol{A} - \boldsymbol{A} \cdot \boldsymbol{W}) + \lambda(\boldsymbol{D} \cdot \boldsymbol{A} + \boldsymbol{A} \cdot \boldsymbol{D} - 2\mathbb{A}:\boldsymbol{D}) + 2\, C_I \dot{\gamma}(\boldsymbol{I} - 3\boldsymbol{A}), \tag{5}$$

where the second- and fourth-order fiber orientation tensors are defined respectively as

$$\boldsymbol{A} = < \boldsymbol{pp} >, \text{ and } \mathbb{A} = < \boldsymbol{pppp} >, \tag{6}$$

Here, $\boldsymbol{p}$ is the unit vector depicting the orientation of a single rigid fiber along the axis of fiber alignment. The angle bracket "< >" refers to an average over all directions, weighted by the probability distribution function of the orientation [11]. λ is a factor counting the geometric effects of the fibers reinforced. For an ellipsoidal fiber, λ can be evaluated as [16]

$$\lambda = \frac{(a_r)^2 - 1}{(a_r)^2 + 1}, \tag{7}$$

where a_r is the hydrodynamic aspect ratio of the ellipsoidal fiber. C_I is an empirical coefficient that including the fiber-fiber interactions. Bay proposed an expression of C_I as [17],

$$C_I = 0.0184 \exp(-0.7148 v_f a_r), \tag{8}$$

where v_f refers to the fiber volume fraction of the composite system. In addition, $\boldsymbol{W}$ and $\boldsymbol{D}$ are the vorticity tensor and rate-of-deformation tensor of the suspension flow, respectively, which can be written as

$$\boldsymbol{D} = (\nabla \boldsymbol{v} + \nabla \boldsymbol{v}^{\boldsymbol{T}})/2 \text{ and } \boldsymbol{W} = (\nabla \boldsymbol{v} - \nabla \boldsymbol{v}^{\boldsymbol{T}})/2, \quad (9)$$

where $\nabla \boldsymbol{v}$ indicates the flow gradient field and the superscript $\boldsymbol{T}$ refers to the matrix transpose operation.

2D Planar Deposition Flow Modeling

This study simulates the LAAM deposition flow by considering the melt flow in the nozzle tip tabular region plus a strand of deposited bead as flow domain of interest. A 2D planar model is employed where the width of extrudate is assumed as in one-unit dimension, as appearing in Figure 2. The diameter of the nozzle tip is 1/8 inch, based on the geometrical design of a Strangpresse large-scale additive manufacturing Model 19 single screw extruder nozzle, as given in [7]. The distance between the nozzle end and material substrate (i.e., layer thickness) is 3mm, as commonly employed in large scale AM applications [12]. In addition, the bead length is set as 30 mm, which is 10 times of the layer thickness so that a quasi-steady state of the fiber orientation could be achieved. The boundary conditions of the flow domain labeled in Figure 2, such that

- Flow inlet, where a fully developed velocity profile is imposed. The velocity profile is computed based on the prescribed volumetric flow rate of $3.05 \times 10^{-4}\ m^3/s$, which is a typical material feed rate in LAAM extruders [12].
- No-slip wall, where $v_t = v_n = 0$, and v_t and v_n refer to the tangential and normal velocity of a node.
- Free surface, where $f_s = f_t = 0$, indicating no pressure condition on the flow end. And f_t and f_n refer to the tangential and normal force of a node.
- Flow end, where geometries contact detection (algorithm provided in Polyflow) is set.
- Material substrate, where a tangent velocity is imposed to simulate the relative motion between the nozzle and the substrate (i.e., v_x = -0.106 m/s, which equals to the averaged vertical velocity of the flow at the nozzle exit, also see [12])

In addition, the hyperbolic form of Equation 5 requires an initial condition of the second-order fiber orientation tensor at the flow inlet. Herein, we imposed a fully developed fiber orientation state reported by Heller, et al. [7], assuming that the orientation state reaches somewhat a steady state at the inlet of the flow. The fiber aspect ratio is set as 15, in an averaged sense, which is a safe estimation based on related experiments (see, e.g., [18,19]). The C_I is set as 0.0055, based on Equation 8.

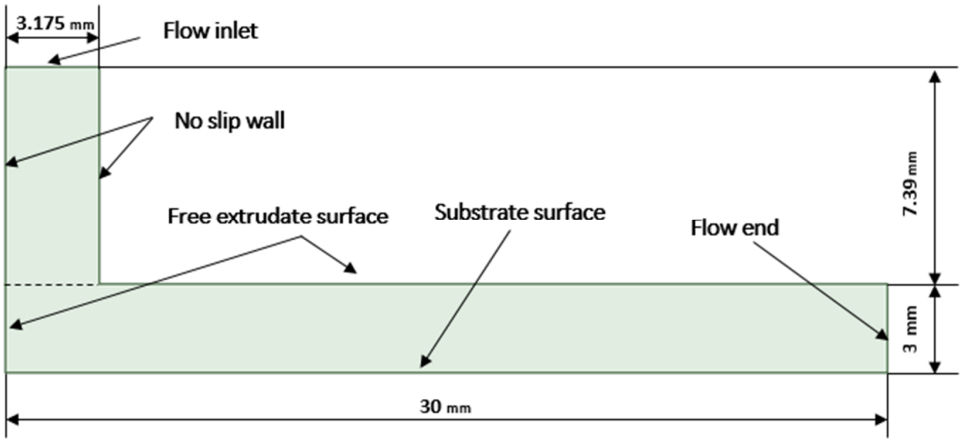

Figure 2. Boundaries of the flow domain of interest.

The flow velocity fields v_x, v_y are plotted in Figures 3 and 4, respectively. It is seen that the velocity profile v_x reaches an equilibrium roughly in the middle of the deposited bead. The fiber orientation tensor fields of A_{11} and A_{22} components are plotted in Figures 5 and 6, respectively. It is clearly seen that the fibers are highly aligned along the direction of deposition. The fiber orientation state also reaches a steady state much faster as compared to the flow kinematics, comparing the contours of Figures 3 and 5. Furthermore, we employed the steady state fiber orientation seen in the flow end to evaluate the material properties through the orientation homogenization method [16]. The second order fiber orientation tensor diagonal components at the flow end across the bead thickness are given in Figure 7. The constituent materials properties of the carbon fiber and PEI matrix are given in Table 1. The computed material properties at each location of the computed fiber orientation tensor (cf. Figure 7) are ultimately integrated across the bead thickness direction to obtain the effective properties of the bead. Computed properties including elastic constants, thermal conductivity and expansion coefficients are given in Table 2. Note, due to the high principal fiber alignment (cf. Figure 5), the material properties of deposited PEI composites exhibit notably material anisotropy. The direction "11" in Table 2 refers to the direction of material loading and "22","33" denote to the transverse directions. In addition, E, α, κ denote to the elastic constant, coefficient of thermal expansion, and coefficient of thermal conductivity, respectively.

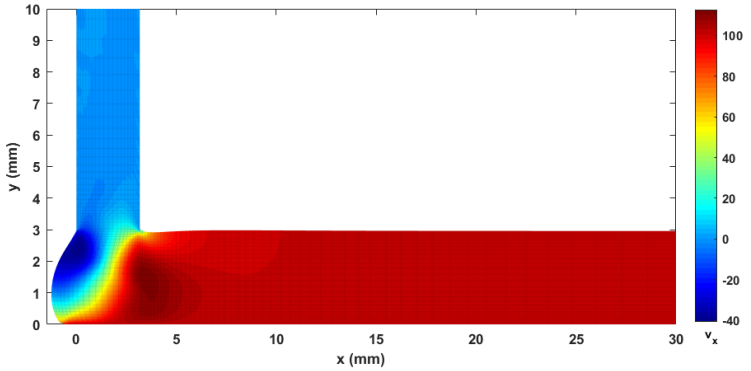

Figure 3. Velocity vector component v_x of planar deposition flow.

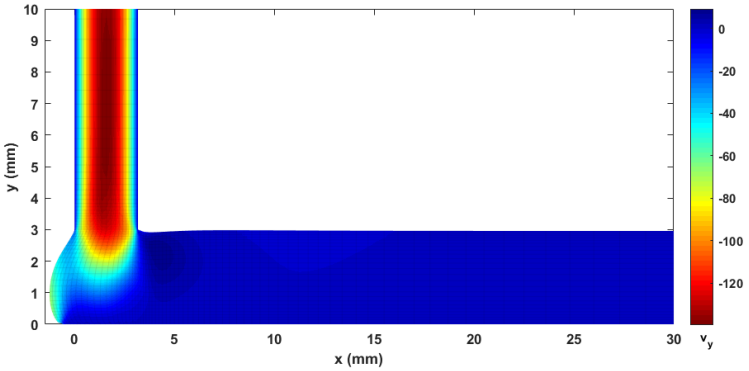

Figure 4. Velocity vector component v_y of planar deposition flow.

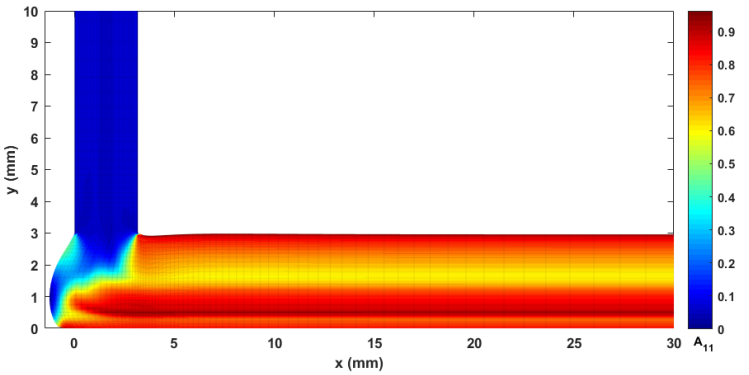

Figure 5. Fiber orientation component A_{11} of planar deposition flow.

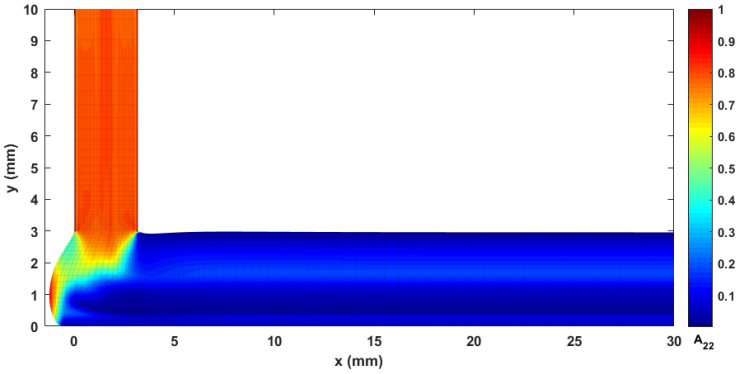

Figure 6. Fiber orientation component A_{22} of planar deposition flow.

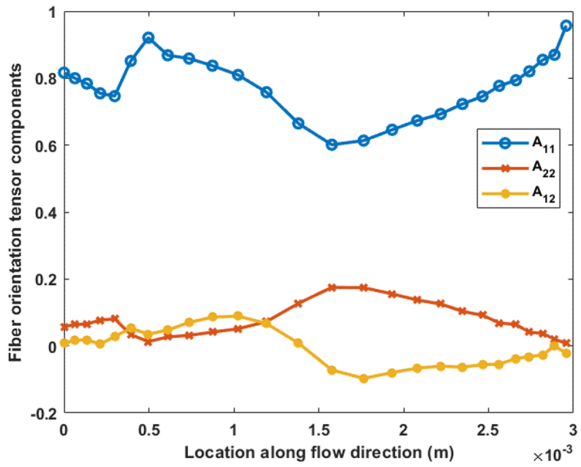

Figure 7. Fiber orientation tensor components at the flow end across the bead thickness.

Table 1. Material properties of the phase materials of a 20 wt.% CF-PEI (~16 vol.%).

Material	**E (GPa)**	$\boldsymbol{\nu}$	α	$\boldsymbol{\kappa}$
PEI matrix	3	0.4	90e-6	0.175
Carbon fiber	230	0.2	-2.6e-6	3.06

Table 2. Material properties of deposited CF-PEI composites estimated by orientation homogenization.

Direction	**E (GPa)**	**G (GPa)**	$\boldsymbol{\nu}$	α	$\boldsymbol{\kappa}$
11	11.67	N/A	N/A	3.084e-5	0.500
22	5.19	N/A	N/A	8.302e-5	0.144
33	1.86	N/A	N/A	7.079e-5	0.182
12	N/A	1.86	0.19	N/A	N/A
23	N/A	1.62	0.52	N/A	N/A
13	N/A	2.19	0.21	N/A	N/A

It is noticed that the steady state fiber orientation at the flow end exhibit notably difference locally, where, e.g., the maximum A_{11} component (i.e., 0.9568) is 59% higher than that of the minimum (i.e., 0.6011). Hoskins, et al. measured the coefficients of thermal expansion on LAAM-made ABS composites and results show a similar trend as seen in A_{11} components appearing in Figure 7. In simulating the residual stress of LAAM-made parts, they partitioned the deposited strand in five subdomains with five different material properties estimated based on their measured data [20]. Herein, a similar strategy is employed to define our deposited PEI composites for further printing process simulation, where the bead is divided into five equal-length sections along the direction of bead thickness. Material properties of each sections are estimated using the local fiber orientation within that section via the same orientation homogenization approach applied above [16]. The entire material properties estimated considering the local fiber orientation state are given in Table 3 for further simulations. Specifically, we plot three properties, for instance, through Figure 8, where the properties of E_{11}, κ_{11}, α_{11}.are included. It can be seen that the locally defined material properties exhibit dramatically differences as compared to the uniformly homogenized

effective properties estimated by the integration over the bead thickness, where the maximum local differences on κ_{11}, and α_{11} are 29% and 21%, respectively.

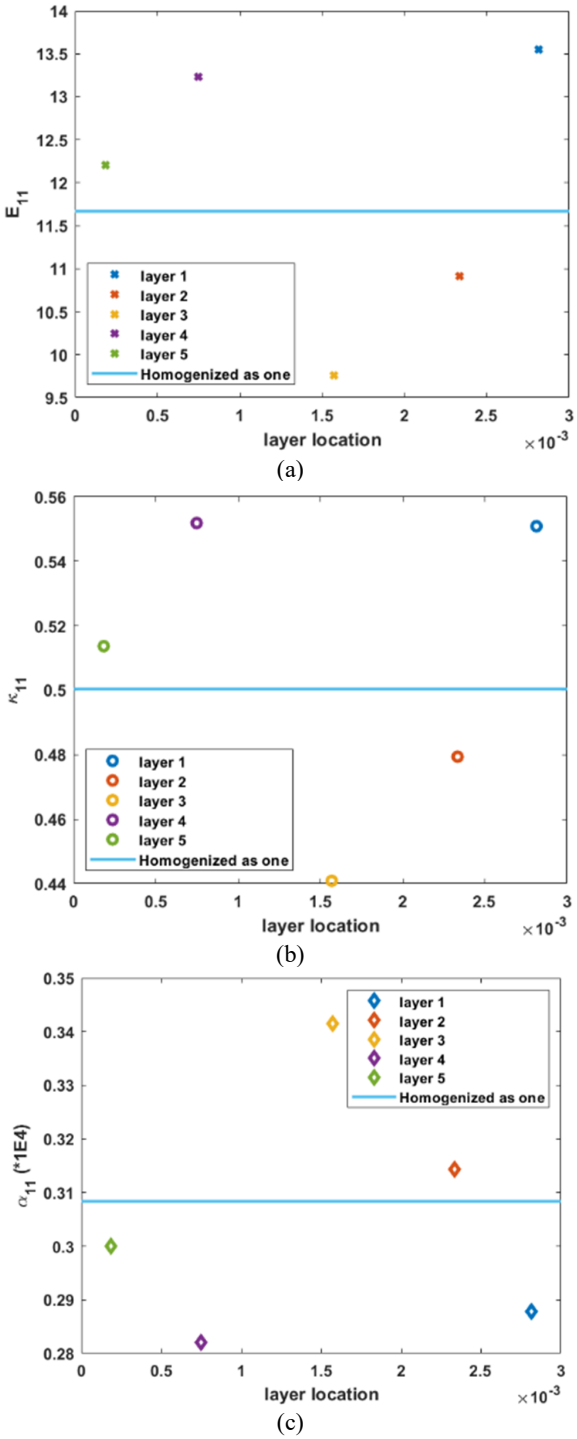

Figure 8. Homogenized material properties across the bead thickness: (a) E_{11}; (b) κ_{11}; (c) α_{11}.

Table 3. Locally homogenized material properties of deposited CF-PEI composites.

Layer	Direction	E (GPa)	G (GPa)	ν	α	κ
Layer 1	11	13.55	N/A	N/A	2.878e-5	0.551
	22	4.70	N/A	N/A	8.660e-5	0.117
	33	4.99	N/A	N/A	7.319e-5	0.158
	12	N/A	1.65	0.16	N/A	N/A
	23	N/A	1.51	0.55	N/A	N/A
	13	N/A	2.06	0.18	N/A	N/A
Layer 2	11	10.91	N/A	N/A	3.144e-5	0.479
	22	4.93	N/A	N/A	8.129e-5	0.156
	33	5.25	N/A	N/A	7.018e-5	0.190
	12	N/A	1.97	0.20	N/A	N/A
	23	N/A	1.68	0.50	N/A	N/A
	13	N/A	2.26	0.22	N/A	N/A
Layer 3	11	9.75	N/A	N/A	3.416e-5	0.441
	22	5.10	N/A	N/A	7.796e-5	0.177
	33	5.44	N/A	N/A	6.803e-5	0.208
	12	N/A	2.09	0.24	N/A	N/A
	23	N/A	1.77	0.49	N/A	N/A
	13	N/A	2.32	0.25	N/A	N/A
Layer 4	11	13.23	N/A	N/A	2.821e-5	0.552
	22	4.67	N/A	N/A	8.708e-5	0.117
	33	4.99	N/A	N/A	7.334e-5	0.157
	12	N/A	1.64	0.16	N/A	N/A
	23	N/A	1.49	0.55	N/A	N/A
	13	N/A	2.05	0.18	N/A	N/A
Layer 5	11	12.20	N/A	N/A	3.000e-5	0.514
	22	4.81	N/A	N/A	8.490e-5	0.134
	33	5.15	N/A	N/A	7.075e-5	0.178
	12	N/A	1.80	0.18	N/A	N/A
	23	N/A	1.59	0.53	N/A	N/A
	13	N/A	2.20	0.20	N/A	N/A

Finite Element Simulation of LAAM

The transient LAAM process of a 100mm-length single strand is simulated via ABAQUS element activation/deactivation function. The unit extrusion element is in 3mm thickness as normally seen for LAAM-deposited beads [11,12]. The width of the unit is assumed as 8mm. The print speed (i.e., nozzle moving speed) is set as 100 mm/s (see, e.g., [11]), and the step analysis time for a unit element is 0.005 second. Thermal and mechanical boundary conditions are set based on a related preceding study [21]. Specifically, the initial temperature of each extrusion unit is 380 ℃, which is common for CF-PEI [18]. The temperatures of the substrate and ambient air are 90 ℃ and 110 ℃, respectively. The air convection coefficient is set as 90 $W/(m^2\ K)$.

Computed Mises stress contours by employing uniformly homogenized material properties and five-layer locally homogenized material properties are given in Figures 9 and 10, respectively.

The stress contours in Figures 9 and 10 are in similar fashion, while the maximum stress values of the simulations exhibit a notable difference. By employing locally homogenized material properties, the maximum stress reduces 14% as compared to that computed using uniformly homogenized material properties. In addition, we present the Mises stress in the direction of material loading in Figures 11 and 12, where significant differences are seen clearly in the contours, especially across the bead thickness. This is a result of the high degree of material anisotropy as seen in Tables 2 and 3. Further, the maximum deformation of the as-printed bead in uniform properties and localized properties simulations are 5.64E-3 mm and 5.13E-3 mm, respectively, i.e., ~10% difference for the LAAM process of a 100mm-length single bead. From where it is expected that for large-dimension LAAM parts, the over-estimation in material deformations may be much higher by using uniformly homogenized properties over locally homogenized properties. To this end, the local orientation effects are considered as a crucial component in simulations of LAAM composites manufacturing.

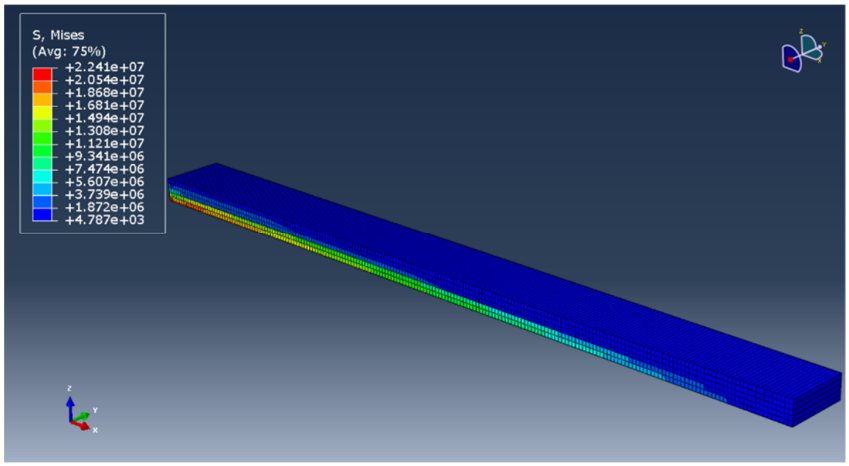

Figure 9. Mises stress contour of a 20% CF-PEI to form a 100mm-length single strand by employing uniformly homogenized material properties.

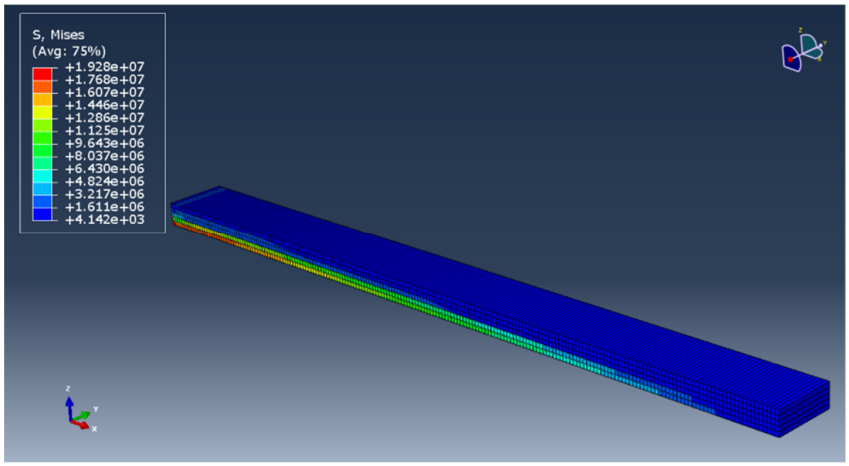

Figure 10. Mises stress contour of a 20% CF-PEI to form a 100mm-length single strand by employing five-layer homogenized material properties.

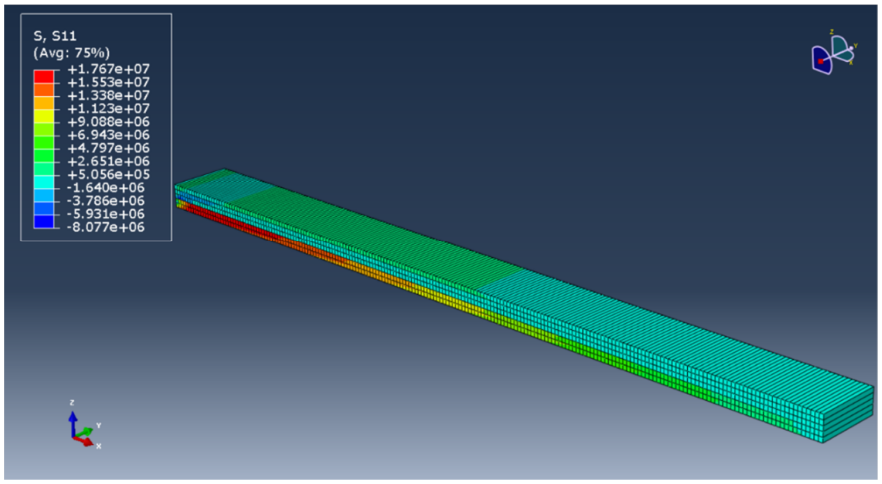

Figure 11. Mises stress component S11 contour of a 20% CF-PEI to form a 100mm-length single strand by employing uniformly homogenized material properties.

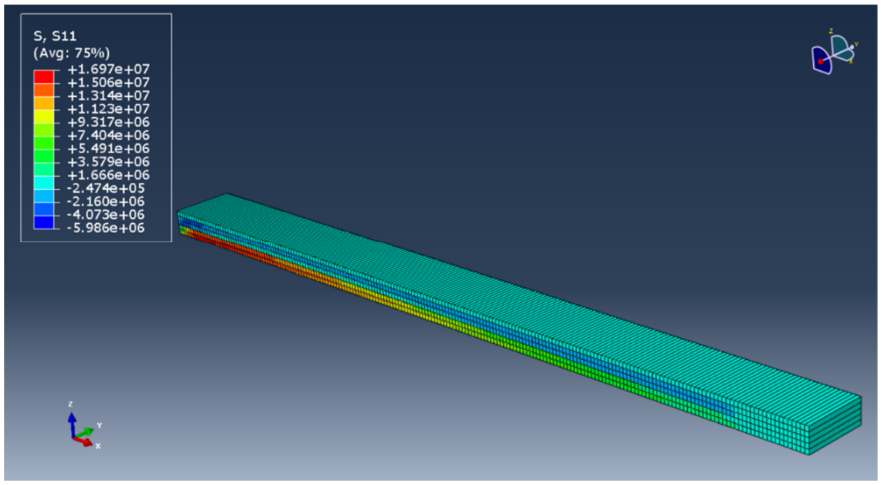

Figure 12. Mises stress component S11 contour of a 20% CF-PEI to form a 100mm-length single strand by employing uniformly homogenized material properties.

Conclusion

A two-step finite element based method is employed to simulation the LAAM process of 20 wt.% carbon fiber filled PEI polymer. The extrusion deposition process is simulated via a fully coupled flow/orientation approach, where the flow kinematics and fiber orientation tensor fields are solved. Employing the steady state fiber orientation tensor at the deposition flow end into the orientation homogenization method, the elastic constants, thermal conductivity and thermal expansion coefficients of the deposited CF-PEI composites are estimated. The fiber orientation effects on the material properties are considered in the property estimations, where the deposited bead is equally divided into five layers and fiber orientation within each layer are homogenized independently. The thermal-mechanical transient history of the LAAM process of a 100mm-length

single deposited strand is simulated via ABAQUS, employing the computed material properties. As compared to results computed by employing uniformly homogenized material properties, the locally homogenized material properties simulation exhibits significant difference in the Mises stress contours, where the maximum stress value reduces 14%. In addition, the uniformly homogenized properties simulation over-estimates the maximum deformation in the deposited bead as compared to the localized properties simulation. To these ends, the fiber orientation effects on the material properties are considered as an important component in LAAM simulations.

Acknowledgements

The authors would like to appreciate the support from Dalian Maritime University and Baylor University. This work was supported by the Fundamental Research Funds for the Central Universities of China (No. 3132021337).

References

[1] Love L J, Duty C E, Post B K, et al. Breaking barriers in polymer additive manufacturing[R]. Oak Ridge National Lab.(ORNL), Oak Ridge, TN (United States). Manufacturing Demonstration Facility (MDF), 2015.
[2] Talagani M R, DorMohammadi S, Dutton R, et al. Numerical simulation of big area additive manufacturing (3D printing) of a full size car. Sampe Journal, 2015, 51(4): 27-36.
[3] Post B K, Chesser P C, Lind R F, et al. Feasibility of using Big Area Additive Manufacturing to Directly Manufacture Boat Molds. Oak Ridge National Lab.(ORNL), Oak Ridge, TN (United States), 2018.
[4] Nieto D M, López V C, Molina S I. Large-format polymeric pellet-based additive manufacturing for the naval industry. Additive Manufacturing, 2018, 23: 79-85.
[5] Peterson E. Technical Challenges to Adopting Large Scale Additive Manufacturing for the Production of Yacht Hulls. International Conference on Human Systems Engineering and Design: Future Trends and Applications. Springer, Cham, 2020: 15-20.
[6] J. Nixon, B. Dryer, D. Chiu, I. Lempert, and D. I. Bigio, "Three parameter analysis of fiber orientation in fused deposition modeling geometries," Annu. Tech. Conf. - ANTEC Conf. Proc., vol. 2, pp. 985–995, Jan. 2014.
[7] Heller B P, Smith D E, Jack D A. Effects of extrudate swell and nozzle geometry on fiber orientation in Fused Filament Fabrication nozzle flow. Additive Manufacturing, 2016, 12: 252-264.
[8] Wang Z, Smith D E. Rheology effects on predicted fiber orientation and elastic properties in large scale polymer composite additive manufacturing. Journal of Composites Science, 2018, 2(1): 10.
[9] Wang Z, Smith D E. Numerical analysis of screw swirling effects on fiber orientation in large area additive manufacturing polymer composite deposition. Composites Part B: Engineering, 2019, 177: 107284.
[10] Bertevas E, Férec J, Khoo B C, et al. Smoothed particle hydrodynamics (SPH) modeling of fiber orientation in a 3D printing process. Physics of Fluids, 2018, 30(10): 103103.
[11] Wang Z, Smith D E. Finite element modelling of fully-coupled flow/fiber-orientation effects in polymer composite deposition additive manufacturing nozzle-extrudate flow. Composites Part B: Engineering, 2021, 219: 10881121.
[12] Wang Z, Smith D E. A Fully Coupled Simulation of Planar Deposition Flow and Fiber Orientation in Polymer Composites Additive Manufacturing. Materials, 2021, 14(10): 2596.
[13] Baird D G, Collias D I. Polymer processing: principles and design. John Wiley & Sons, 2014.
[14] G.B. Jeffery. The motion of ellipsoidal particles immersed in a viscous fluid. Proc. R. Soc. London, Ser. A, 102 (715) (1922), pp. 161-179.

[15] F. Folgar, C.L. Tucker III. Orientation behavior of fibers in concentrated suspensions. J. Reinf. Plast. Compos., 3 (2) (1984), pp. 98-119.
[16] S.G. Advani, C.L. Tucker III. The use of tensors to describe and predict fiber orientation in short fiber composites. J. Rheol., 31 (8) (1987), pp. 751-784.
[17] Bay, R.S. Fiber Orientation in Injection-Molded Composites: A Comparison of Theory and Experiment. Ph.D. Thesis, Univer-sity of Illinois at Urbana-Champaign, Champaign, IL, USA, 1991.
[18] Ajinjeru C, Kishore V, Chen X, et al. Rheological survey of carbon fiber-reinforced high-temperature thermoplastics for big area additive manufacturing tooling applications. Journal of Thermoplastic Composite Materials, 2019: 0892705719873941.
[19] Wang Z, Smith D E, Jack D A. A statistical homogenization approach for incorporating fiber aspect ratio distribution in large area polymer composite deposition additive manufacturing property predictions. Additive Manufacturing, 2021, 43: 102006.
[20] Hoskins, Dylan, et al. "Modeling thermal expansion of a large area extrusion deposition additively manufactured parts using a non-homogenized approach." Proceedings of the SFF Symposium (2019)
[21] Zhang Y, Chou Y K. Three-dimensional finite element analysis simulations of the fused deposition modelling process. Proceedings of the Institution of Mechanical Engineers, Part B: Journal of Engineering Manufacture, 2006, 220(10): 1663-1671.